NANO · MICRO
small

Supporting Information

for *Small*, DOI 10.1002/smll.202302355

Fano-Like Resonance from Disorder Correlation in Vacancy-Doped Photonic Crystals

*Jose Angel Pariente, Farzaneh Bayat, Alvaro Blanco, Antonio García-Martín, Carlos Pecharromán, Manuel I. Marqués and Cefe López**

Fano-Like Resonance from Disorder Correlation in Vacancy-Doped Photonic Crystals (Supplementary information)

Jose Angel Pariente,[1] Farzaneh Bayat,[1,2] Alvaro Blanco,[1] Antonio García-Martín,[3] Carlos Pecharomán,[1] Manuel I. Marqués,[4] Cefe López[1*]

*[1]Instituto de Ciencia de Materiales de Madrid (ICMM); Consejo Superior de Investigaciones Científicas (CSIC) Calle Sor Juana Inés de la Cruz 3, E-28049 Madrid Spain, *c.lopez@csic.es;*
[2] Department of Physics, Azarbaijan Shahid Madani University (ASMU), Tabriz, 53751-71379, Iran;
[3] IMN-Instituto de Micro y Nanotecnología (CNM), Consejo Superior de Investigaciones Científicas (CSIC) Isaac Newton 8 (PTM), E-28760 Tres Cantos, Madrid, Spain;
[4] Departmento de Física de Materiales & Condensed Matter Physics Center (IFIMAC) & Nicolás Cabrera Institute, Universidad Autónoma de Madrid (UAM), Av. F. Tomás y Valiente, Cantoblanco 28049 Madrid, Spain

S1. Sample preparation

The vertical deposition method[1] makes it possible to obtain the photonic self-assembled nanostructures. High-quality opals with a large homogeneous *fcc* lattice and an appreciable thickness are obtained with this method. In order to grow the opals a colloidal suspension of 0.15 wt% in 10 mL is prepared and the evaporation rate is controlled in a climate chamber by adjusting the temperature and relative humidity to 45° C and 20 %, respectively, for 48 hours. The opals are built by mixing two different types of monodisperse dielectric spheres in the colloidal suspension which are Polymethyl Methacrylate (PMMA) and Polystyrene (PS). Statistical analysis of the images of the Scanning Electron Microscope (SEM) reveals a diameter of $d = 334$ nm and d = 313nm for PMMA and PS, respectively, with a 3% of polydispersity in both cases. The small difference in the size (~6% just above the polydispersity) does not have any negative effect on the growth. of opal as can be seen in **Fig.** S1a where the outer surface of a mixed opal prior to PS removal is shown. We assess the impact of such size mismatch on optical quality by comparing the reflectance of alloys with different concentration of PS spheres before selectively removing them and there were no significant changes. A much larger size mismatch was demonstrated to be tolerable for the fractions studied in this work.[2]

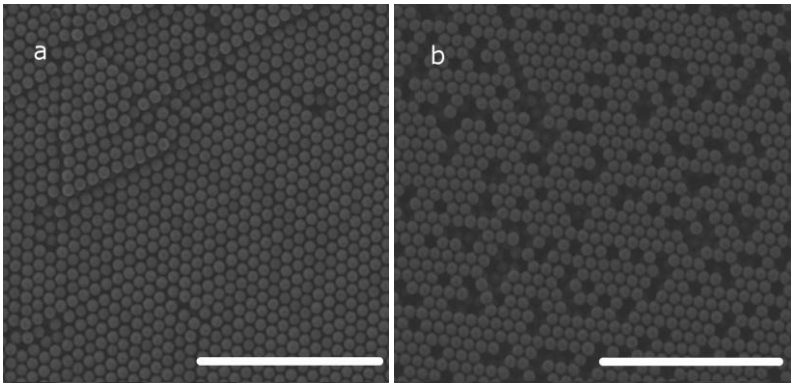

Figure S1. SEM images of an opal with 18% of PS dopants before (a) and after (b) the selective removal. The chemical selective etching by cyclohexane does not affect the PMMA spheres providing an easy procedure to make vacancies (Scale bar 5 micrometres)

The PS has been removed from the opal by a selective chemical etching. A typical SEM image of the structure's outer surface after removing PS is shown in **Fig.** S1b. In particular, PS selective removal is performed by immersing the samples in 99% pure cyclohexane for 24 hours. This is a very simple procedure that completely removes PS spheres from their lattice positions, leaving the PMMA spheres undisturbed.

S2. Optical Properties

Optical spectra are collected with a Bruker FTIR coupled to an optical microscope using a 4× objective to keep the beam nearly collimated and with an aperture that limits the field to a circle of 180 μm diameter. Notice that for a 20-layer sample of 300 nm diameter spheres this volume comprises 5.4 million spheres which warrants a good statistical average in the plane while the systems remain essentially finite in the perpendicular direction. Light is collected at normal incidence, coinciding with the ΓL direction of the reciprocal space, for different numbers of layers.

Regions of increasing thickness can be clearly distinguished as a colour code topographic map under the microscope; simply by counting the terraces on the VPhC from the edge of the sample, one can locate regions of the desired thickness because each terrace increases the number of layers by one.

An alternative, equally easy, and independent method involves fitting the maxima of the Fabry-Perot fringes. A rough estimate of Bragg wavelength based on the average refractive index predicts a decreasing behaviour of the Bragg wavelength that is not observed in the experiments for concentration as high as 10% or more because, in the case presented, the slightly smaller size compensates for the larger refractive index. This method provides a fine control not only on the fraction of vacancies, but also on the thickness.

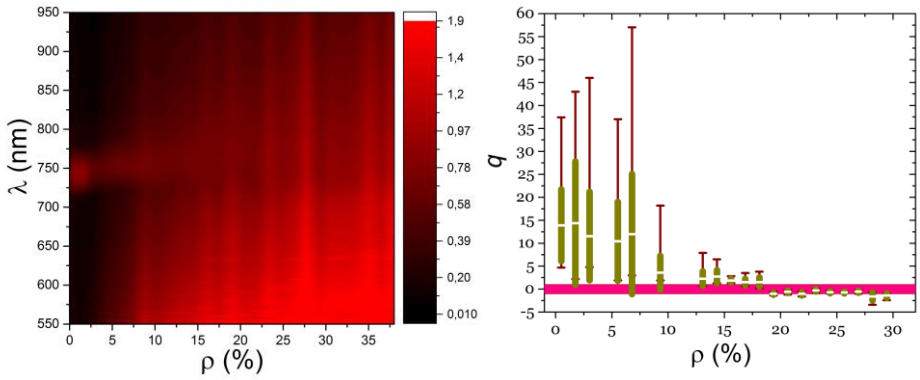

Figure S2. Surface contour plot of the transmittance (absorbance) spectra at the normal incidence (left) and fit q parameter (right) of different VPhC between 0% and38% vacancies for 20 layers. The brown whiskers represent the maximum and minimum value obtained for the *q* parameter. The boxes are the standard deviation and the white lines are the mean from the values. At the percolation threshold the *q* parameter are in the shaded pink area which are values of the *q* parameter between $-1 < q < 1$, close to zero.

By means of collecting the light at the normal incidence, reflectance and transmittance spectra are measured in the band gap direction. In Fig. S2, transmittance spectra of different VPhC for 20 layers are shown. As a result of adding vacancies, an increase in the diffusive light is seen agreeing with the description of the *q* parameter made in the main article. In order to obtain the *q* parameter from the transmittance spectra, we use the absorbance (– log *T*) obtained from samples with varying vacancies concentrations and thicknesses. The description of the *q* parameters obtained for the absorbance spectra shares the same view as in the reflectance spectra (**Fig.** S2, right). However, in this case, fitting of the spectra beyond $\rho = 30\%$ is not possible due to the large contribution of the diffusive scattering which masks the optical features of the spectra.

S4. Finite size effects

The photonic properties of the systems are strongly dependent on thickness due to finite size effects. It is therefore necessary to account for the behaviour of the *q* parameter versus sample thickness (**Fig.** S3). The build-up of a photonic band gap is hardly complete for thicknesses below or about the Bragg length ℓ_B, which is the distance over which light attenuates by a factor of *e* at the band gap. This corresponds to the light black shaded area in **Fig.** S3. It should be natural to expect that the importance of the discrete channel grows steadily only up to this value.

For a few layers thicknesses, the band structure of the VPhC has a broad gap (much like quantum confinement broadens semiconductor gaps). By increasing the thickness, the band gap becomes narrower and extinction increases (and so does reflectance). In these circumstances, the broad background scattering is dominant and *q*, therefore, small. By increasing sample thickness, the gap acquires definition and Bragg scattering gains strength and the discrete channel outweighs background Mie scattering so that *q* grows. The *q* parameter reaches a maximum for the Bragg length (ℓ_B). In our case, we measure a $\ell_B = 1.9$ μm that corresponds to 8 monolayers. This is the minimum thickness necessary to define the photonic bands and gap. For these thicknesses no proper bands are defined and scattering is dominated by single (Mie) scattering. The more layers are included the better the photonic band structure is defined and the less importance scattering acquires. Therefore, the *q* parameter increases with thickness. We speculate that beyond that point *q* decreases because the number of defects even for undoped samples (and naturally, for low percentage of vacancies) has been observed to increases with thickness.[3]

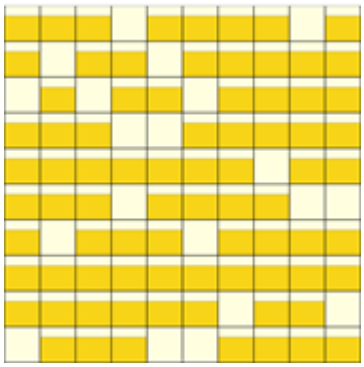

Figure S1 | Schematic representation of a 10×10 cells (black boundaries) of the PhC including 20% of vacancies. Each cell can be either occupied by a sphere (deep yellow) leaving 26% void (light yellow) in the interstices or empty, in which case all 100% of the cell is empty (light yellow).

Above ℓ_B (8 layers) the q parameter decays until it reaches a stationary value. This decay is due to the transition to an infinite crystal. The band gap and the diffusion scattering background change with the thickness of the crystal. As the background of diffusion is increased, a finite value for q parameter will be obtained. When we have an infinite crystal (beyond 25 layers), the band gap and the scattering does not change anymore. In other words, the optical properties of an infinite photonic crystal do not depend on the thickness. As a result of this fact, the q parameter reaches a stationary value.

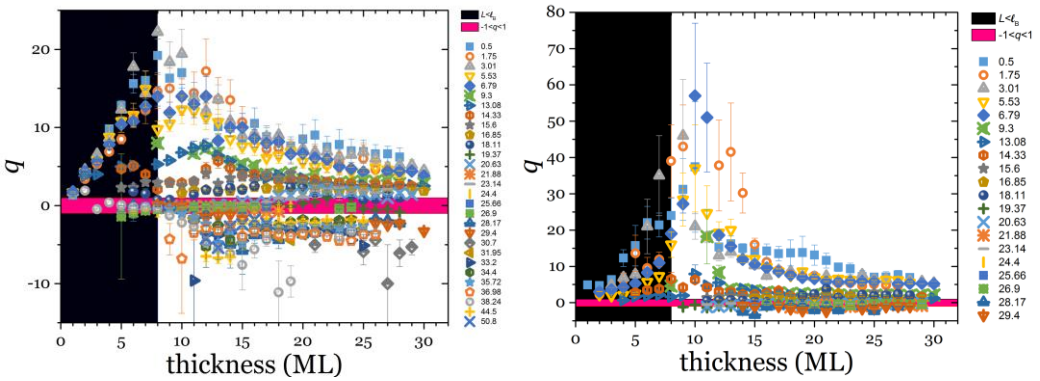

Figure S3 q parameter as a function of the thickness for different VPhC for reflectance (left) and absorbance (right) spectra. The shaded black area are the first layers in which the VPhC have neither a well-defined band gap nor the underestimated surface effects. Thus, a trustworthy q parameter is not obtained for these first layers and we can neglect it. When the volume of the VPhC can be considered infinite, the q parameter tends to a value depending on the number of vacancies.

The same behaviour in the transition to an infinite crystal can be observed for the VPhC above the percolation threshold. However, in this case the description for ℓ_B cannot be applied because crystal size is more and more restricted by the increasing amount of vacancies: notice that below 8 monolayers with over 20% vacancies leaves little chance to form sizable crystals and consequently only diffuse scattering can be expected.

S5 Analytical modelling

In the simplest approximation, for a plane wave travelling along the Z direction, assuming the string lies on the Z-axis, the reflected electromagnetic field at $z = -\infty$ is given by $E \propto \sum_{i=1}^{N} \alpha_i e^{-\iota 2kz_i}$ with ι the imaginary unit, z_i the positions of the i-th dipole and $k = 2\pi/\lambda$ being the wave number in vacuum of the incoming radiation. The optical paths (refractive index multiplied by the effective geometrical path) across a scatterer and a dopant are given by their optical sizes, $d_s = D\, n_s$ and $d_d = D\, n_d$ respectively, where D is the lattice spacing resulting from the sphere size. Notice that, even if particles and defects cells are of the same size (required for a good crystalline quality) their optical size is different. If two random particles are nearest neighbours, the optical path form centre to centre is given by d_s with probability $(1-\rho)^2$ (scatterer-scatterer), d_d

with probability ρ^2 (dopant-dopant) and $(d_s + d_d)/2$ with probability $2\rho(1-\rho)$ (scatterer-dopant or dopant-scatterer). A crude model is depicted in **Fig**. S4.

The phase at z_i, the "i-th" element, depends on the optical path accumulated by the previous constituents and given by

$$z_i = \left[\frac{d_1+d_i}{2} + \sum_{j=2}^{i-1} d_j\right] \tag{1}$$

The reflected intensity, $I \propto \mathbf{E}^* \cdot \mathbf{E}$, is given by

$$I \propto \sum_{i=1}^{N} [\alpha_i]^2 + 2\sum_{j>i} \alpha_i^* \alpha_j \cos\left(2k(z_j - z_i)\right) \tag{2}$$

Let us now consider the average over many different columns, with different random distributions of dopants all characterized by the same dopant density, incoherently contributing to the backscattering. That is, let's assume that for each sample region the field is the vector sum form the stacked layers' contributions (according to their phase) and that regions contribute to the intensity independently. Then, the reflected intensity will be given by averaging over many realisations of the summation in Eq. (2):

$$\langle I \rangle \propto \langle \sum_{i=1}^{N} |\alpha_i|^2 \rangle + 2\,\langle \sum_{j>i}^{N} \alpha_i^* \alpha_j \cos\left(2k(z_j - z_i)\right)\rangle \tag{3}$$

which, taking into account the definition of covariance between two random variables, $\mathrm{cov}(X,Y) = \langle XY\rangle - \langle X\rangle\langle Y\rangle$, assigning $X = \{\alpha_i \alpha_j\}$, and $Y = \left\{\cos\left(2k(z_j - z_i)\right)\right\}$ the total intensity can be separated into two terms $\langle I\rangle \propto I_{\mathrm{sym}} + I_{\mathrm{cov}}$ with designations (*symmetric* and *covariance*) justified below.

$$I_{\mathrm{sym}} = \langle \sum_{i=1}^{N} |\alpha_i|^2 \rangle + 2\sum_{i<j} \langle \alpha_i^* \alpha_j \rangle \langle \cos[2k(z_i - z_j)]\rangle \tag{4}$$

and

$$I_{\mathrm{cov}} = 2\sum_{i<j} \mathrm{cov}\{\alpha_i^* \alpha_j, \cos[2k(z_i - z_j)]\} \tag{5}$$

In order to estimate the averages involving cosines it is necessary to compute the distribution of optical paths. Let $m = (j-i)-1$ be the number of positions between i-th and j-th scatterers. Since the probability that m' out of m ($m' \leq m$) are occupied by defects is given by the binomial distribution:

$$P(m,m') = \binom{m}{m'} \rho^{m'} (1-\rho)^{m-m'} \tag{6}$$

The optical path between two different cells will be $m' d_{\mathrm{d}} + (m - m') d_{\mathrm{s}}$ with probability $P(m,m')$. Therefore, considering the three different possibilities for the values of $\alpha_i{}^* \alpha_j$ we obtain:

$$\langle \cos[2k(z_i - z_j)]\rangle = (1-\rho)^2 T_{\mathrm{ss}}^{ij} + \rho^2 T_{\mathrm{dd}}^{ij} + 2\rho(1-\rho) T_{\mathrm{sd}}^{ij} \tag{7}$$

with $T^{ij} \equiv T^{i-j}$ since T's only depend on the diference $i-j$

$$T_{\mathrm{ss}}^{ij} = \sum_{m'=0}^{m} P(m,m') \cos[2k(m' d_d + (m-m') d_s + d_s)] \tag{8}$$

for cases where both i and j are spheres,

$$T_{\mathrm{dd}}^{ij} = \sum_{m'=0}^{m} P(m,m') \cos[2k(m' d_d + (m-m') d_s + d_d)] \tag{9}$$

when both are defects, and

$$T_{sd}^{ij} = \sum_{m'=0}^{m} P(m,m') \cos\left[2k\left((m' d_d + (m-m') d_s) + \left(\frac{d_s + d_d}{2}\right)\right)\right] \tag{10}$$

if i and j are different (one defect and one sphere).

With this we can write analytical expressions for *sym* contribution to the reflected intensity as:

$$I_{\mathrm{sym}} = N\langle|\tilde{\alpha}|^2\rangle + 2|\langle\tilde{\alpha}\rangle|^2 \sum_{i<j}(1-\rho)^2 T_{ss}^{ij} + \rho^2 T_{dd}^{ij} + 2\rho(1-\rho)T_{sd}^{ij} \tag{11}$$

with $\langle|\tilde{\alpha}|^2\rangle = (1-\rho)|\,\tilde{\alpha}_s|^2 + \rho|\tilde{\alpha}_d|^2$ and $|\langle\tilde{\alpha}\rangle|^2 = (1-\rho)^2|\,\tilde{\alpha}_s|^2 + \rho^2|\tilde{\alpha}_d|^2 + 2\rho(1-\rho)\Re(\,\tilde{\alpha}_s\tilde{\alpha}_d{}^*)$ being $\tilde{\alpha}_s, \tilde{\alpha}_d$ the polarizabilities of scatter and dopant respectively and $\Re(\,\tilde{\alpha}_s\tilde{\alpha}_d{}^*)$ the real part of the product of effective polarizabilities

For ($d_d/d_s \sim 1$) and assuming both polarizabilities are real, the *sym* term can be approximated by the functional form:

$$I_{\mathrm{sym}} \approx N\sigma_\alpha^2 + |\langle\tilde{\alpha}\rangle|^2 \left[\frac{\sin(kNd)}{\sin kd}\right]^2 \tag{12}$$

with $d = \langle d\rangle = (1-\rho)d_s + \rho d_d$the average optical size, and $\sigma_\alpha^2 = \langle|\tilde{\alpha}|^2\rangle - |\langle\tilde{\alpha}\rangle|^2$ the polarizability variance. I_{sym} contains a constant background intensity, proportional to the variance of the polarizability, plus the Bragg diffraction line-shape coming from a homogenous PhC with polarizability and particle optical size given by the averaged values. This is the typical spectrally *symmetric* response of a regular periodic structure hence the designation.

The second term (I_{cov}) arises from the *covariance* between phases and polarizabilities' products in the column hence the designation. Both quantities are correlated because the phase accumulated between two elements in the stack depends on how many constituents of each kind (scatterers or dopants) there are in between. Using the definition $\mathrm{cov}[X,Y] = \langle(X-\langle X\rangle)\times(Y-\langle Y\rangle)\rangle = \langle(X-\langle X\rangle)\times Y - (X-\langle X\rangle)\times\langle Y\rangle\rangle$ the *i-j* elements in the summation giving I_{cov} from Eq. (5) can be written as:

$$\mathrm{cov}\{\alpha_i^*\alpha_j, \cos[2k(z_i - z_j)]\} = \langle[\alpha_i^*\alpha_j - \langle\alpha_i^*\alpha_j\rangle]\cos[2k(z_i - z_j)]\rangle - \langle[\alpha_i^*\alpha_j - \langle\alpha_i^*\alpha_j\rangle]\langle\cos[2k(z_i - z_j)]\rangle\rangle \tag{13}$$

Of the two terms, the second one can be cancelled since, $\langle\cos[(z_i - z_j)2k]\rangle$ can be taken out in the averaging process, leaving $\langle\alpha_i^*\alpha_j - \langle\alpha_i^*\alpha_j\rangle\rangle$ which is identically zero.

Then, from the first term, and considering that *i-j* corresponds to *d-d* (two defects) with probability ρ^2, *s-s* (two spheres) with probability $(1-\rho)^2$ and *s-d* (one defect and one sphere) with $2\rho(1-\rho)$, using the averages $\langle|\tilde{\alpha}|^2\rangle = (1-\rho)|\tilde{\alpha}_s|^2 + \rho|\tilde{\alpha}_d|^2$ and $|\langle\tilde{\alpha}\rangle|^2 = (1-\rho)^2|\tilde{\alpha}_s|^2 + \rho^2|\tilde{\alpha}_d|^2 + 2\rho(1-\rho)\Re(\tilde{\alpha}_s^*\tilde{\alpha}_d)$, and performing the summation, we obtain:

$$I_{\mathrm{cov}} = 2\sum_{i<j}(1-\rho)^2(|\tilde{\alpha}_s|^2 - |\langle\tilde{\alpha}\rangle|^2)T_{ss}^{ij} + \rho^2(|\tilde{\alpha}_d|^2 - |\langle\tilde{\alpha}\rangle|^2)T_{dd}^{ij} + 2\rho(1-\rho)(\Re(\tilde{\alpha}_s^*\tilde{\alpha}_d) - |\langle\tilde{\alpha}\rangle|^2)T_{sd}^{ij} \tag{14}$$

This contribution to the reflectance is an asymmetric function that changes its asymmetry when $|\langle\tilde{\alpha}\rangle|^2$ has a minimum, similar to what a Fano function does with q, where it adopts an inverted Lorentzian line shape. Note how, for $\tilde{\alpha}_s = \tilde{\alpha}_d$ or $d_s = d_d$, the covariance term exactly vanishes ($I_{\mathrm{cov}} = 0$)

S5 Graphical link between field enhancement and critical concentration

It is interesting to plot the critical defect concentration vs. the field enhancement. The numerical expression of equation (18) in the main text is

$$\rho_c = \frac{-0.125 + 0.260\gamma}{0.615 - 1.480\gamma + \gamma^2} \tag{15}$$

As this equations, for FCC PhC structure has not parameters, a simple curve links the critical density with field enhancement.

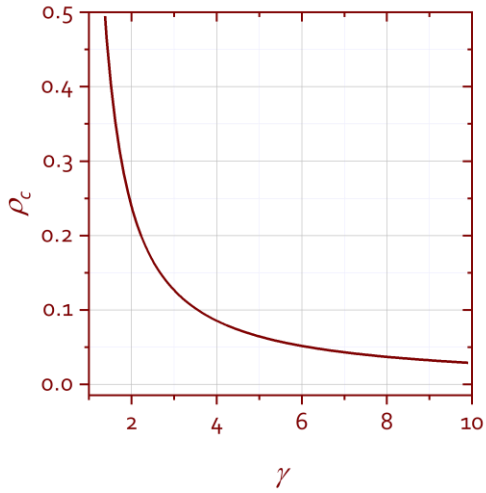

Figure S5 Critical density at which the Fano parameter changes sing as a function of electromagnetic field enhancement.

The first important conclusion is that as the enhancement grows the critical concentration of vacancies drops to zero (Seen in Fig. S5.) As can be seen all dependence of the critical density is on the field enhancement, which, in turn, for a given lattice, will only depend on the refractive index contrast. Note how, when $\gamma = 1$ (no field enhancement) the critical density is equal to one.

Numerical simulations

The numerical simulations have been performed using a commercial Finite Difference Time Domain (FDTD) solver for Maxwell's equations (Lumerical®). We use an impinging Gaussian beam wave with polarization along the X-axis and propagating along the Z-axis (perpendicular to the sphere (111) plane). It is launched at 8 μm from the substrate, and parametrized using the built-in scalar approximation: (Beam size and divergence angle: beam radius $w_z = 5$ μm, divergence angle 4 degrees). The geometry of the cell (9.6 μm × 8.59 μm × 19.52 μm) and the size of the launching Gaussian beam makes it possible to consider an almost homogeneous field in the PC area. We use a refined mesh in the nanostructures and in near field region (3 μm × 3 μm × 6.1 μm) of 7.5 nm × 7.5 nm × 7.5 nm, dx-dy-dz, respectively. Outside this region the mesh is allow to grow uniformly up to a maximum of 27 nm close to the simulation boundaries, so that convergence (to the best of our numerical capabilities) is attained. The PC is modelled as a stack of layers 20 by 37 n=1.5 nanospheres with d=330nm (totalling 740 nanospheres), laying on top of a SiO2 substrate.

We have used these simulations to compute the enhancement factors that can be extracted from representations like Fig. 6a in the main text and the following that correspond to λ = 680, 700, 745, and 760 nm.

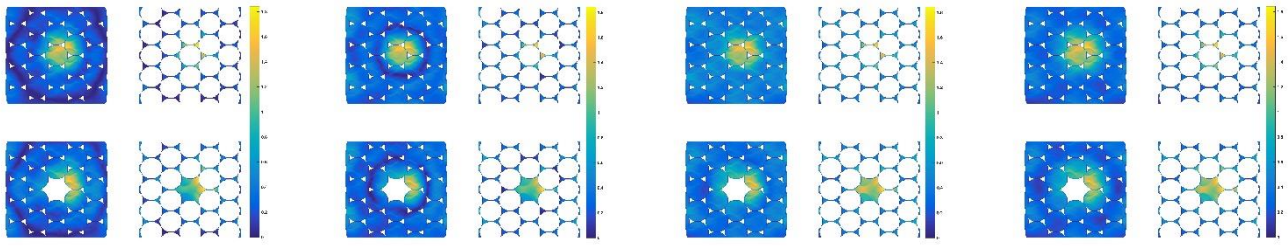

680 nm 700 nm 745 nm 760 nm

References

1 Jiang, P. & Bertone, J. Single-crystal colloidal multilayers of controlled thickness. Chem. Mater. 11, 2132–2140 (1999).
2 Palacios-Lidón, E., Juárez, B. H., Castillo-Martínez, E. & López, C. Optical and morphological study of disorder in opals. J. Appl. Phys. 97, 1–7 (2005).
3 Galisteo-López, J., Palacios-Lidón, E., Castillo-Martínez, E. & López, C. Optical study of the pseudogap in thickness and orientation controlled artificial opals. Phys. Rev. B 68, 1–8 (2003).